Accepted Article Preview: Published ahead of online publication

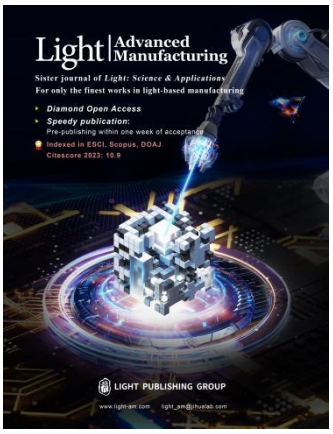

Integrated Digital Metasurface-Enabled Agile Wireless Power Transfer System

Hao Zhang, Zhenyuan Li, Yuxuan Deng, Yuhua Chen, Xilong Lu, Zhenfei Li, Yue Yin, Li Sun, Xudong Bai

Cite this article as: Hao Zhang, Zhenyuan Li, Yuxuan Deng, Yuhua Chen, Xilong Lu, Zhenfei Li, Yue Yin, Li Sun, Xudong Bai. Integrated Digital Metasurface-Enabled Agile Wireless Power Transfer System. *Light: Advanced Manufacturing* accepted article preview 10 June, 2026; doi: 10.37188/lam.2026.097

Received 20 May 2025; Revised 5 June 2026; Accepted 10 June 2026;
Accepted article preview online 10 June 2026

Integrated Digital Metasurface-Enabled Agile Wireless Power Transfer System

Hao Zhang[1], Zhenyuan Li[1], Yuxuan Deng[1], Yuhua Chen[1], Xilong Lu[1], Zhenfei Li[2], Yue Yin[1,*], Li Sun[1,*], and Xudong Bai[1,*]

[1] School of Integrated Circuit, Northwestern Polytechnical University, Xi'an, 710129, China

[2] School of Physical Science and Technology, Northwestern Polytechnical University, Xi'an 710129, China

* baixudong@nwpu.edu.cn

* yinyue@nwpu.edu.cn

* lisun@nwpu.edu.cn

Abstract

Recent advancements in smart manufacturing demand wireless power transfer (WPT) systems with dynamic adaptability and miniaturised receivers; however, existing solutions suffer from narrow operational bandwidths and inflexible spatial energy distributions. In this paper, we present a digital metasurface-driven WPT platform that synergises surface plasmon-enhanced coupling with advanced low-temperature cofired ceramic (LTCC) microfabrication. The meta-atom is designed with a wideband configuration and optimised via the magnetoelectric dipole coupling theory. This can enable 180°±5° phase modulation over a 22% fractional bandwidth (5.0–6.25 GHz) and achieve adaptive impedance matching under varying load conditions. A multi-target WPT system is further demonstrated by integrating a digital metasurface, dynamically controlled in real time via a field-programmable gate array, as the energy source, and employing rectennas as receivers corresponding to multiple target positions. The system enables the dynamic shaping of the electromagnetic energy distribution through beam reconfiguration, thus achieving highly directional pencil beams with millisecond-level reconfigurability. The LTCC-based rectenna, leveraging multilayer plasmonic ceramic structures, can attain an RF-to-DC efficiency of 70.5% at 5.8 GHz within an 18 mm×18 mm footprint. Thus, it resolves the efficiency degradation in miniaturised receivers. Experimental results demonstrate that, compared with static metasurface schemes, the proposed system can dynamically switch beam angles and the number of targets in real time, significantly enhancing the spatial energy coverage while maintaining full compatibility with 5G NR standards. This system may pioneer a manufacturing-compatible framework for intelligent metasurface-enabled WPT systems in Internet of Things (IoT) applications.

Keywords: Metasurface, Low-Temperature Co-fired Ceramic (LTCC), Wireless Power Transfer (WPT), Rectenna

Introduction

With the rapid expansion of Internet of Things (IoT) devices and the arrival of 5G/6G wireless networks, the demand for wireless power transmission (WPT) systems has surged[1,2]. Particularly in emerging fields such as smart cities, industrial automation, and remote healthcare, the widespread deployment of these devices presents new and significant challenges[3-5]. A key requirement for supporting the continuous operation of these devices is the provision of reliable and sustained power. Current wireless power technologies must address the efficient delivery of power across multiple dimensions, including space, time, and spectrum, while also accommodating large-scale, multi-target, and high-speed transmission requirements[6-8]. However, traditional WPT systems encounter numerous bottlenecks, including uneven spatial energy distribution, low power transfer efficiency, challenges in multi-target energy delivery, limited system bandwidth, and complex hardware architectures[9-11]. These challenges significantly hinder the scalability and practical application of traditional systems, particularly when addressing dynamic environmental changes and evolving demands.

Metasurface technology has emerged as a promising solution to address these challenges and has attracted increasing interest[12-17]. With their subwavelength-scale ability to control electromagnetic (EM) waves, metasurfaces can precisely manipulate EM wave propagation properties[18-24], including reflection, refraction, scattering, and polarisation, thus offering more flexible and efficient solutions for WPT systems[25,26]. Recent advancements in metasurface technology have led to significant progress in the research on WPT systems. For example, multi-target energy transfer systems based on anisotropic metasurfaces[27] and magnetic induction-powered base station designs using nonlinear metasurfaces[28] have demonstrated the tremendous potential of metasurfaces to surpass the efficiency limits of traditional WPT systems. However, most metasurfaces employed in early WPT systems relied on passive devices, which typically exhibited static characteristics, making them unsuitable for handling

dynamically changing environments[29]. This limitation also creates significant challenges in achieving broadband energy harvesting, enhancing spatial power density, and improving system integration, all of which require further innovations to overcome these barriers.

Research on WPT metasurfaces has advanced by integrating active devices to drive technological progress, and dynamic control architectures based on PIN diodes and field-programmable gate arrays (FPGAs) have significantly improved the system response time. For example, branch-and-bound optimisation algorithms have been proposed for a multiple-input–multiple-output energy transfer system utilising a digital metasurface; it was experimentally validated for multiuser energy efficiency and fairness[30]. An innovative shared-aperture metasurface achieved wide-angle radio frequency (RF) to direct-current (DC) conversion efficiency of over 50% within an incident angle of 45°, and its compact design provides new insights for system integration[31]. This breakthrough also includes a dual-frequency adaptive wireless power network, which can achieves 3-cm positioning accuracy and a rectification efficiency of 61% in the near field by employing spatiotemporal coding and deep learning collaboration[32]. A parallel innovation is related to the passive information-energy metasurface, which can achieve an energy capture efficiency of 76% at 4.1 GHz and synchronously decouple the control information from the energy supply through beam scanning 5.8 GHz[33]. Another advancement in digital metasurface-enabled WPT systems is the utilization of joint waveform optimisation to improve the average rectification efficiency to 76%, while simultaneously achieving multi-beam scanning for near-field focusing at 6 GHz[34]. Despite these advancements, existing technologies still encounter key challenges, such as broadband efficiency decay, nonlinear harmonic suppression, and collaborative optimisation of distributed networks[35-37]. Another key constraint is that the profile of conventional digital metasurfaces requires further reduction because they have a relatively high profile as a result of an external feed source, which is also a key constraint for achieving

compact WPT systems[38-40]. Therefore, efficient low-profile metasurface architectures and high-performance multi-target energy transfer systems are urgently required.

However, the design of miniaturised and highly -efficient wireless power receiving units is a critical technological challenge in ensuring the stable operation of various IoT devices[41-43]. The energy-receiving module typically consists of an antenna and rectifier, which are commonly co-designed and referred to as the rectenna. However, conventional rectennas are typically fabricated using high-frequency organic substrates, which typically have bulky dimensions and are unsuitable for flexible IoT applications[44,45]. Miniaturised design indicators may also substantially deteriorate the RF-to-DC conversion efficiency[46,47]. The emergence of low-temperature co-fired ceramic (LTCC) technology can provide innovative solutions for rectenna design and WPT construction because the LTCC dielectric has exceptional RF performance and exhibits high permittivity and ultralow dielectric losses, which can provide fundamental advantages for developing compact rectennas with high conversion efficiency[48-50].

In this paper, we propose an integrated digital metasurface-enabled agile multi-target WPT system. Additionally, a novel LTCC-based rectenna architecture was specifically designed for integration with compact IoT devices, thus enabling the efficient conversion of RF energy emanating from the metasurface. The core innovations of our proposed design include two aspects: **First, a low-profile wideband integrated digital metasurface topology:** Through the integration design of a microwave excitation network along with the metasurface radiators, the proposed wideband integrated digital metasurface avoids the external space-feed source required by its traditional counterpart. Thus, it overcomes the limitations of leakage radiation and achieves a very low profile of less than 0.1 λ_0. **Second, an ultra-compact high-efficiency rectenna design:** Through a multilayer LTCC process, an 18 mm × 18 mm miniature rectenna was designed and fabricated, achieving a maximum RF-to-DC conversion efficiency of 70.5% at a central frequency of 5.8 GHz. By integrating a low-profile integrated metasurface with an LTCC rectenna, the WPT system can ensure stable energy transmission in multi-user scenarios within the 5G NR protocol frequency bands. This system may overcome the

bottleneck of static metasurface power transfer efficiency, thereby providing a new paradigm for constructing highly adaptive wireless power networks and advancing the practical deployment of self-powered IoT systems.

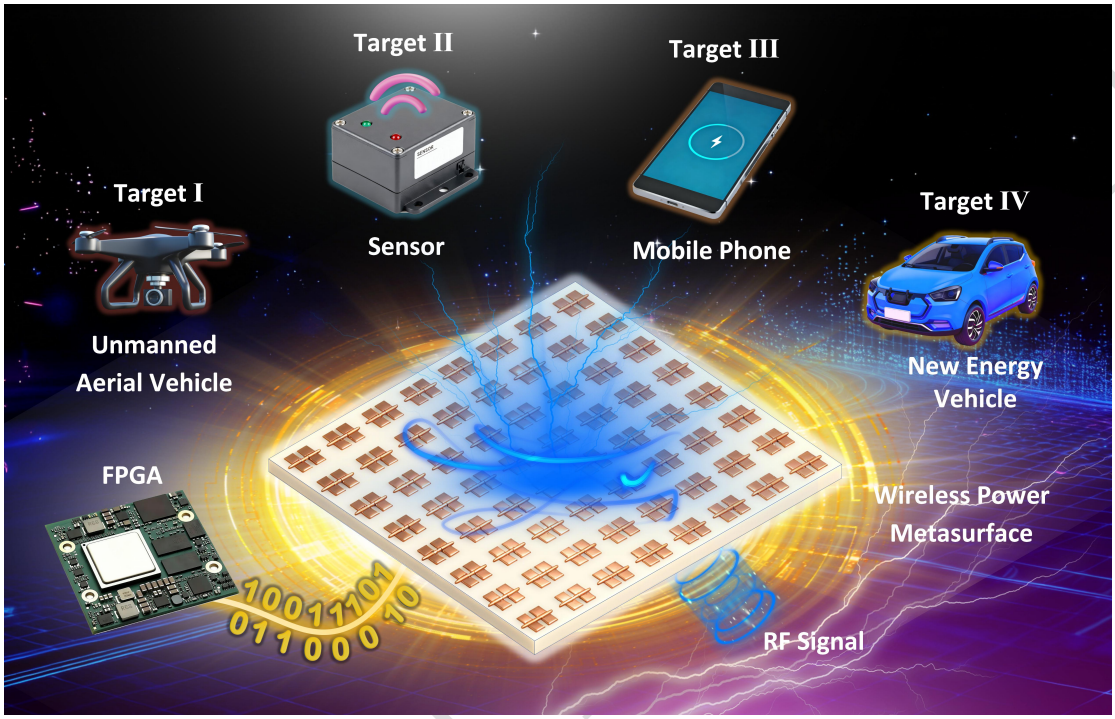

Figure 1. Schematic of the multi-target wireless energy transfer metasurface architecture. The metasurface is stimulated via a feeding network and regulated by computer-controlled FPGA input encoding, thus enabling multi-target energy transmission. Its application scenarios include drones, sensors, mobile phones, and new energy vehicles, addressing the demand for smart interconnected multi-target energy transfer for various modern IoT applications.

Results

The architecture of the entire WPT system comprises two main modules. The energy transmission module employs an integrated digital metasurface that is dynamically and reconfigurably controlled in real time via an FPGA, thereby enabling both single-target and multi-target wireless energy delivery. Multiple rectennas are utilised on the receiving end to emulate various targets and effectively harvest the transmitted energy. In practical applications, these rectennas can be integrated into unmanned aerial vehicles, sensors, and new-energy vehicles, thus offering flexible and long-range alternatives to conventional wired charging. The detailed architecture

of the multi-target WPT metasurface system is illustrated in **Fig. 1**.

I. Digital Metasurface Design

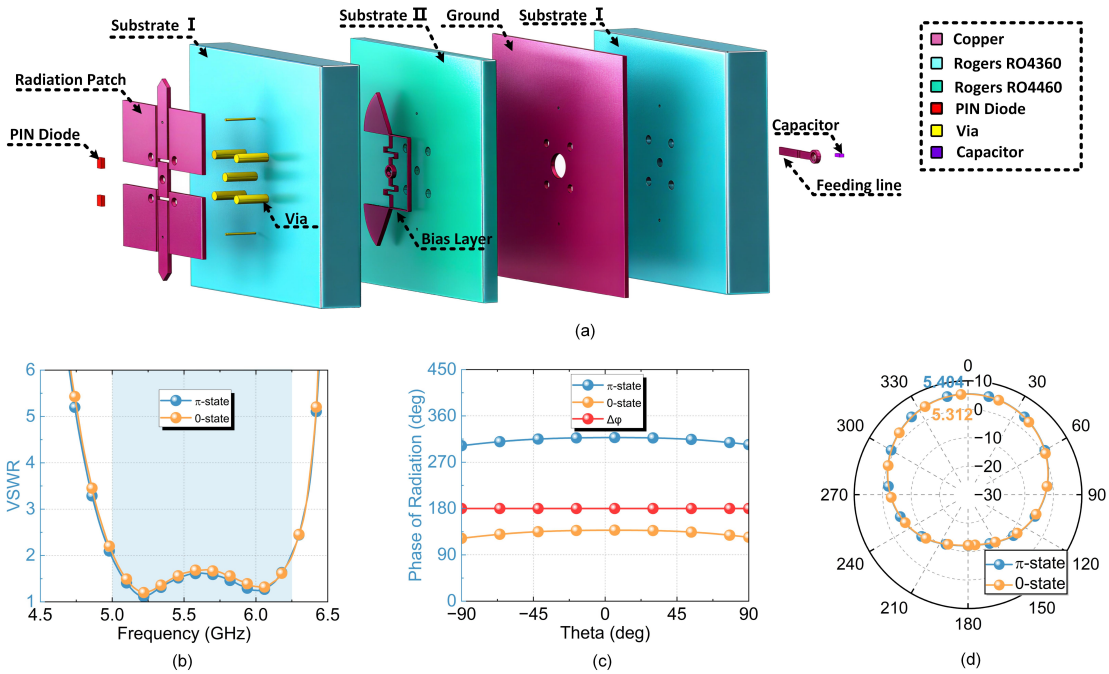

Figure 2. Integrated meta-atom structure (a) and performance at 5.8 GHz (b–d). a, Exploded view of the energy transmission meta-atom. **b**, VSWR of the meta-atom. **c**, Phase and phase difference of the meta-atom in two different states. **d**, Radiation gain 2d polar plot of the meta-atom in two different states.

Based on the magnetoelectric dipole coupling theory, the designed meta-atom configuration includes three substrate and four metal layers, as shown in **Fig. 2**. The substrates used are Rogers RO4360 with a dielectric constant of ε_r = 6.15 and Rogers RO4460 with ε_r = 6.15. The metal layers include a top radiation layer, biasing layer, metal ground, and feeding layer. The top radiation layer is composed of four quadrate patches with metallised grounding via-holes. Wideband impedance matching for the feed of the meta-atom is achieved by employing a central-axis T-shaped probe to stimulate the meta-atom radiator. The period of the meta-atom is set as 25 mm × 25 mm, which is less than half of the wavelength within the operation frequency band, thus suppressing the sidelobes of the radiation energy after conducting the metasurface array layout. The detailed parameters of each meta-atom layer are shown

in **Fig. S1**.

The central feed probe of the meta-atom integrates two MACOM MADP-000907-14020 PIN diodes, with an ON-state resistance of 5.2 Ω and OFF-state capacitance of 0.025 pF, which are dynamically connected to an RLC bias network composed of fan-shaped capacitors and serpentine inductors via high-density metallised vias (with diameters of 0.25 mm). This forms a tuneable circuit, thus enabling the meta-atom to achieve two phase states with a phase difference of 180°. The current distributions of the meta-atoms in the two states are shown in **Fig. S1**. The feeding network layer innovatively introduces a microstrip line structure combined with a DC blocking capacitor to suppress DC interference and reduce insertion loss. The ground layer was designed with a large area to prevent radiation energy from interfering with the normal operation of the feeding network, thereby further improving the energy transmission efficiency. The overall structure of the meta-atom is shown in Fig. 2a.

Within the effective working frequency band from 5 to 6.25 GHz, the designed meta-atom demonstrates outstanding performance with a simulated VSWR less than 2, as shown in Fig. 2b, which satisfies the high-density communication and power transmission requirements with a wide fractional operation bandwidth of approximately 22%. Through the switching of the PIN diode states, the radiation phase is precisely controlled within 180° ± 5° at 5.8 GHz, as shown in Fig. 2c, with phase error below 3%, satisfying the binary encoding accuracy requirement. Fig. 2d shows the 2D polar radiation patterns of the two different states, with gains of 5.312 and 5.404 dBi, respectively. The radiation patterns exhibit excellent EM performance for wavefront manipulation, and the high gain and low loss lay the foundation for subsequent metasurface arraying layouts.

The configuration of the 8×8 integrated metasurface array is illustrated in Fig. 3a–c. The radiating patch layer consists of 64 meta-atoms and 128 PIN diodes for digital phase encoding with overall dimensions of 200 mm × 200 mm. The biasing network

layer is divided into four subregions, each containing 16 atoms that are independently controlled via dedicated connectors. A left-right symmetrical bias-line layout was adopted to minimise signal attenuation and simplify the wiring design. The feeding network layer incorporates an in-phase, equal-amplitude architecture based on impedance transformation and Wilkinson power-divider principles, ensuring a uniform power distribution across all meta-atoms while maintaining a low insertion loss.

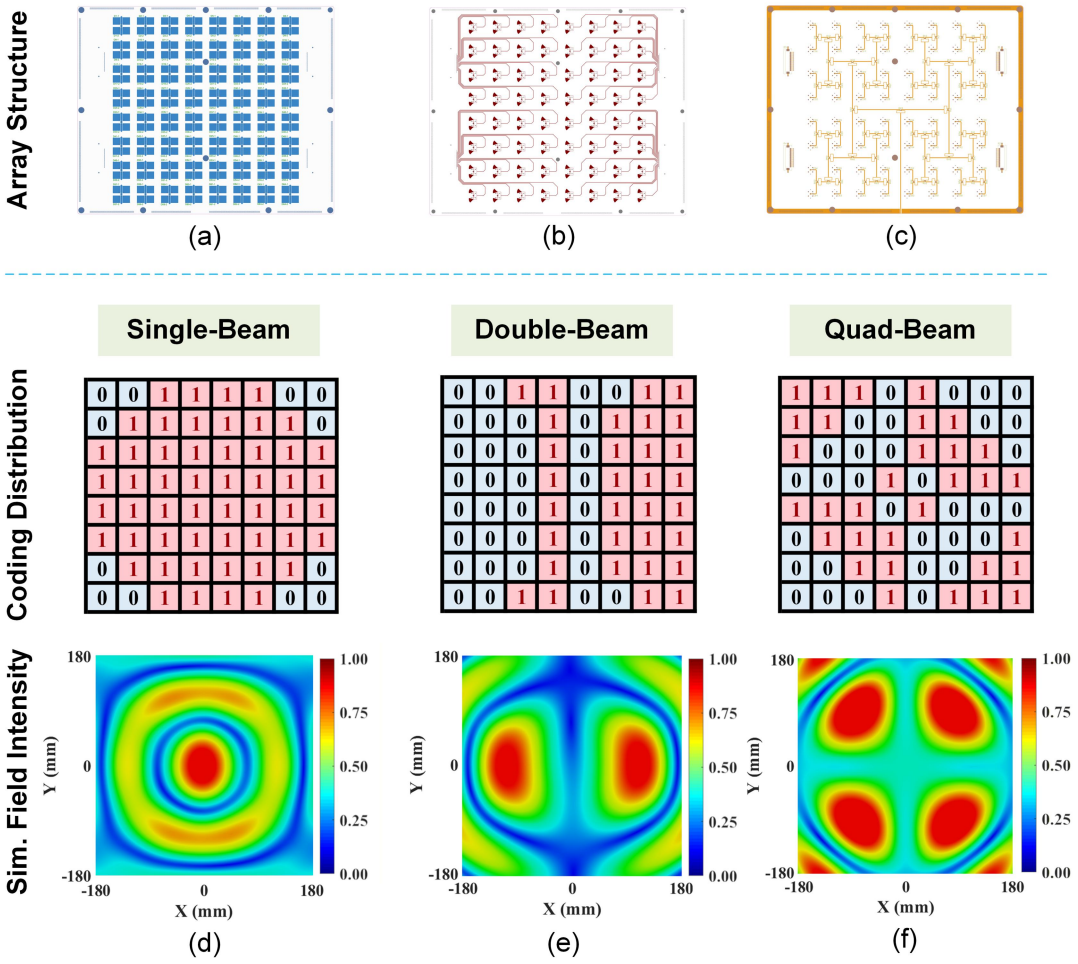

Figure 3. Integrated metasurface array structure (a–c), and quantized phase coding distributions for near-field beam generation of the metasurface with the corresponding 2D near-field patterns located at 40 cm away from the metasurface (d–f). a, Metasurface radiation patch layer. **b**, Metasurface bias network layer. **c**, Metasurface feed network layer. **d**, Single-beam near-field focusing distribution and normalized simulated field intensity. **e**, Dual-beam near-field focusing distribution and normalized simulated field intensity. **f**, Quad-beam

near-field focusing distribution and normalized simulated field intensity.

Based on joint simulations and optimisations using CST Microwave Studio and MATLAB, an equal-amplitude in-phase feeding network was further combined with the designed meta-atoms to construct a multi-objective energy transmission system by adopting real-time FPGA encoding[51]. The phase-quantised coding distribution of the metasurface array and the corresponding 2D near-field patterns are depicted in Fig. 3d–f. The focal spot is located approximately 40 cm from the metasurface. By utilising FPGA-based control for metasurface coding, the designed metasurface can generate single, dual, or quad beams with high beam-steering accuracy and isolation. More detailed information on the far-field beam profiles and corresponding gain distributions generated by the metasurface array is provided in Fig. S2. These results confirm that the proposed metasurface energy transmission system can achieve simultaneous energy delivery to multiple targets in the near-field region, highlighting its promising applications in multi-target intelligent interconnected networks.

II. Rectenna Design and Fabrication

A receiving rectenna was designed to verify that the metasurface can transmit energy to multiple targets simultaneously. It was fabricated through the LTCC process with Ferro-A6M green tape as the dielectric substrate. Ferro-A6M exhibits excellent high-frequency characteristics, an exceptionally low dielectric loss ($\tan\delta$ = 0.002), and stable permittivity ($\varepsilon_r = 5.9 \pm 0.1$) across frequency range of 1–100 GHz, thereby effectively minimising signal transmission loss while enhancing both antenna radiation efficiency and power conversion efficiency of the rectification. A 32-layer green tape stacking configuration was implemented, with each layer maintaining a precise thickness of 96 μm. This multilayer architecture with a high permittivity enables a compact rectenna design with dimensions of only 18 mm × 18 mm. Compared with conventional printed circuit board (PCB)-based implementations (e.g. Rogers 4350B substrate with ε_r = 3.66, typically requiring

minimum dimensions of 30 mm × 30 mm), the LTCC process rectenna represents a minimum reduction in the physical footprint of 60%. Furthermore, the LTCC substrate demonstrates enhanced thermal management capabilities, which facilitate efficient heat dissipation, thus effectively mitigating the performance degradation from RF-to-DC rectification caused by the temperature-dependent impact. The combination of these material properties and structural innovations has facilitated the development of high-efficiency microwave power transmission systems.

As illustrated in **Fig. 4a**, its laminated structure integrates 33 layers of Ferro-A6M green tape, with each layer measuring 96 μm in thickness and exhibiting a dielectric constant ε_r of 5.9 and loss tangent tanδ of 0.002 at 5.8 GHz. The LTCC structure is fabricated through a series of steps, including slicing, punching, via filling, printing, lamination, isostatic pressing, hot cutting, binder burnout, co-firing, and dicing. Prefabricated multilayer green tapes with interlayer interconnects and metallised patterns are stacked in a specific order. This stack is then transformed into a monolithic body through the application of heat and pressure, and is ultimately sintered at peak temperatures ranging from 850 to 1000 °C. The rectenna consists of three functional components: a top layer consisting of a radiating patch, an embedded air cavity, and aperture coupling to capture electromagnetic energy from the metasurface; a mid-layer with a feeding network to convert and propagate RF signals through transmission lines; and a bottom-layer rectification system for RF-to-DC power conversion. The radiation layer utilizes 10-layer laminated green tapes to achieve an enhanced operational bandwidth. An air cavity is formed by selectively removing the ceramic from 11-layer green tapes, with precisely rounded edges to minimise the stress concentration during the co-firing process. The embedded air cavity enhances the bandwidth and radiation efficiency of the antenna with an optimised size of 14 mm×14 mm. The radiation layer and the air cavity are fabricated independently and subsequently soldered together. The feed layer is composed of two four-layer of green tapes (totalling eight-layer tapes). The

aperture-coupled structure isolates the feeding network from the radiation patch. An H-shaped slot is designed to increase coupling between the feed and radiation layers. The RF signal is coupled to a stripline (SL) feeder and transmitted to the rectifier through a vertical coaxial-type stripline-to-microstrip line (MSL) transition, enabling broadband vertical transmission and three-dimension (3D) integration. The implementation of a stripline feeding structure effectively suppresses electromagnetic coupling and enhances the isolation between the antenna and rectifier. The fabricated LTCC rectenna is shown in Fig. 4b and had dimensions of 18 mm×18 mm. The S-parameter (S_{11}) of the antenna was simulated and is presented in Fig. 4c; it demonstrated satisfactory impedance matching from 5.7 to 5.9 GHz. The far-field radiation patterns in Fig. 4d demonstrate a gain of 5.83 dBi, with 3-dB beamwidths of 92.9° in the xoz plane and 97.7° in the yoz plane, achieving a radiation efficiency of 90.2%.

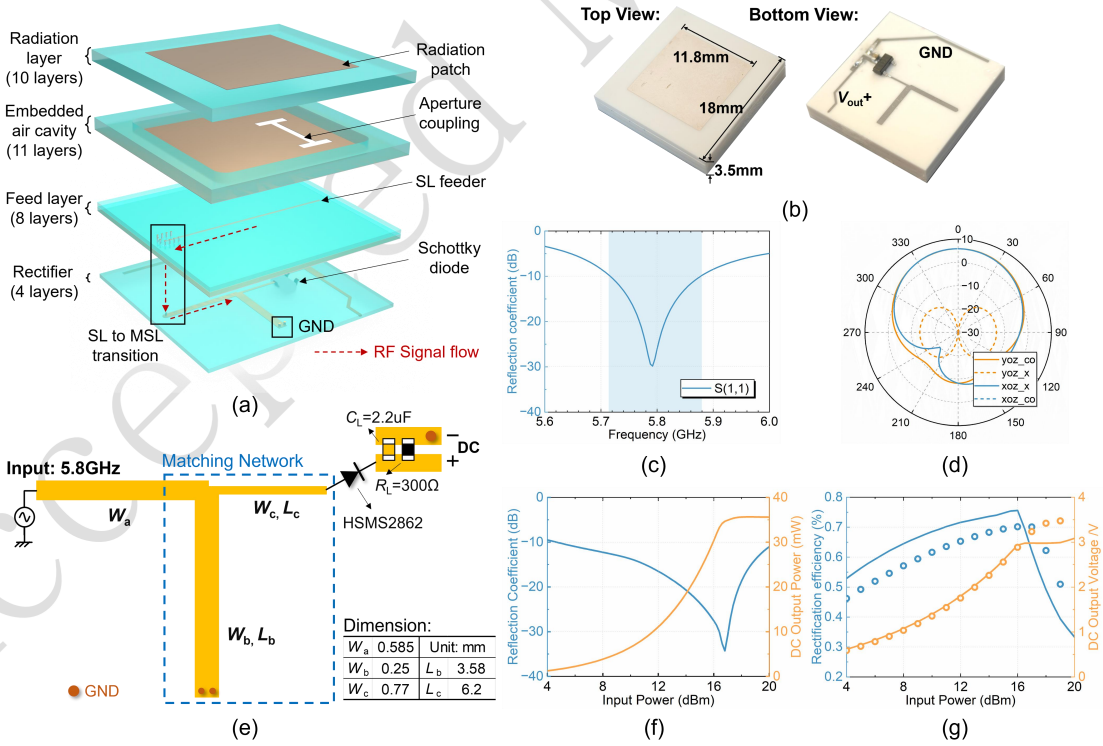

Figure 4. Structural diagram and fabricated prototype of the rectenna (a-b), performance of the antenna at the centre frequency of 5.8 GHz (c-d), and layout and performance of rectifier circuit (e-f). a, Exploded view of the rectenna. **b**, Fabricated prototype of the antenna. **c**,

Reflection coefficient S_{11} at the operating frequency. **d**, 2D radiation pattern of the antenna. **e**, Layout of the rectifier with dimensions. **f**, Reflection coefficient S_{11} and DC output power versus input power. **g**, Simulated and measured rectification efficiency and DC output voltage of the rectifier versus input power.

The structural configuration and design parameters of the rectifier are shown in Fig. 4e, where the RF signal from the antenna SL feeder is input through an impedance-matching network to the Schottky diode (HSMS2862, Avago, Inc.) for rectification. The rectifier was designed with four-layer green tapes at the bottom of the rectenna. The simulated reflection coefficient of the rectifier (Fig. 4f) demonstrated that almost all the RF power can be efficiently received and rectified (S_{11} < -10 dB, input power from 4 to 20 dBm). Fig. 4g depicts a measured maximum RF-to-DC conversion efficiency of 70.5% at an input power of 16 dBm at 5.8 GHz and more than 60% efficiency across the 9–18 dBm dynamic range.

III. Construction of the Wireless Power Transfer System

To verify the effect of dynamic wireless power transfer, we constructed an integrated digital metasurface-enabled WPT system. The system setup and experimental environment are depicted in **Fig. 5a**. A signal generator (SG) (Ceyear 1435F) and a power amplifier (PA) were used as the feed to generate a 5.8 GHz 36 dBm power signal. The prototype of the energy transmission metasurface had dimensions of 200 mm× 200 mm and was composed of 64 meta-atoms, as shown in Fig. 5b. The rectennas were placed 40 cm from the geometric centre of the metasurface to receive the beam power. The received power is the free-space RF power captured by the receiving antenna and is inferred from the DC output of the rectenna. The measured DC output voltage and calculated receiving RF power of the antennas in the single-, dual-, and quad-beam generation scenarios are summarised in Fig. 5c. In the single-beam mode, the output voltage was approximately 2.6 V with a corresponding received power of approximately 15 dBm. In the dual-beam mode, the output voltages were measured approximately 1.60 V, corresponding to a

received power of approximately 11 dBm. This configuration reflected the half-power distribution between the two beams. In quad-beam mode, the output voltages of the rectennas were approximately 1.15 V, corresponding to a received power of about 8.5 dBm. This demonstrates that the designed integrated metasurface can effectively divide power into four portions in the quad-beam mode.

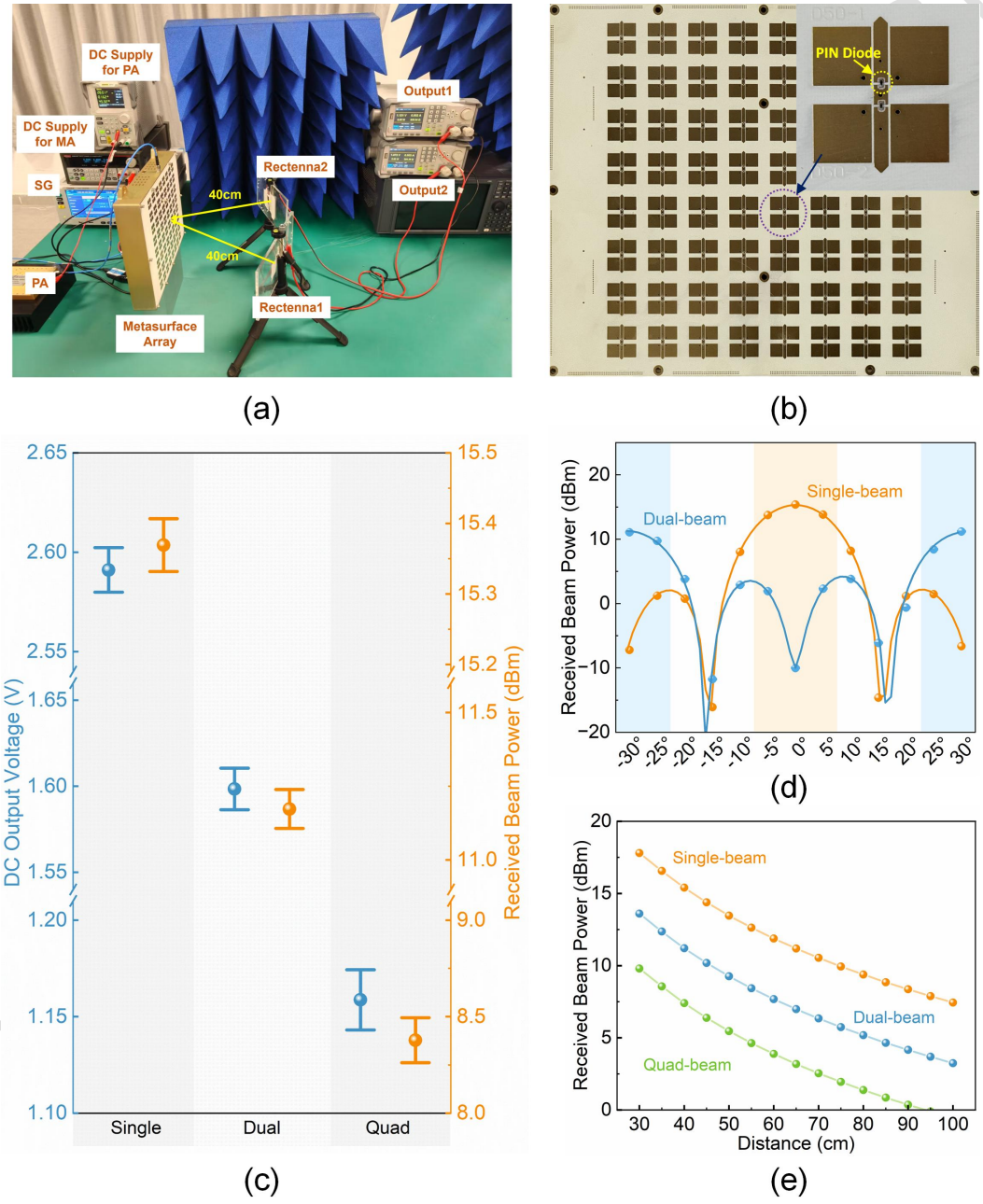

Figure 5. Experiments and results of the dynamic beam control wireless power transfer system. a, Experimental setup for quad-beam generation of wireless power transfer with two

receiving rectennas. **b**, Fabricated metasurface array (MA). **c**, Statistical results of DC output voltage and received beam power under different beam modes. **d**, Measured received beam power of rectenna under different angles in single- and dual-beam modes with a relative distance of 40 cm. **e**, Measured received beam power of rectenna under different distance in different beam modes.

The received beam power in single- and dual-beam modes under at angles between -30° and 30° at a distance of 40 cm were measured and are shown in Fig. 5d. In the single-beam mode, it had a maximum power between -5° and 5°. In the dual-beam mode, two maximum power receiving points were observed, which were approximately at -30° and 30°, respectively. The received beam powers in different modes at different distances between the metasurface and rectenna were measured and are depicted in Fig. 5e. For each distance, the receiving angle and height of the rectenna were optimally adjusted, and the maximum output voltages were recorded after numerous tests. The received power data were then calculated based on the measured relationship between the input power and efficiency of the rectifier (Fig. 4g), which provided reference data for scenarios at different locations of the IoT receiver devices to adjust the working state and output power of the metasurface.

Table 1 Performance comparison between the proposed digital metasurface and existing digital metasurfaces

Ref.	Mode of operation	Element number	Gain (dBi)	Aperture efficiency	Bandwidth	Profile
[18]	Reflection	20×20	24.2	20.9%	6.9%	$12\lambda_0$
[52]	Reflection	16×16	22.0	24.5%	9.5%	$7.1\lambda_0$
[33]	Transmission	20×20	26.3	34%	8.4%	$5\lambda_0$
[53]	Transmission	20×20	22.5	10.52%	28.6%	$0.16\lambda_0$

[34]	Radiation	260	22.54	21.45%	13.3%	$0.09\lambda_0$
This work	Radiation	8×8	20.6	68.0%	22%	$< 0.1\lambda_0$

Table I compares the performances of the proposed and existing digital metasurfaces. Benefiting from the adoption of an equal-amplitude and in-phase feeding network instead of a conventional external feed source, the proposed design effectively eliminates feed blockage, thereby significantly improving aperture efficiency. The aperture efficiency values were calculated from the experimentally measured gain data reported in the respective references using the same definition and calculation method adopted in this work[54]. Moreover, the integrated configuration reduced the overall profile height substantially, enhancing the practicality and suitability of the system for engineering implementation. However, despite these advantages, several challenges remain unresolved. The current metasurface still exhibits limited phase resolution, which may result in slight beam-pointing deviations. Future research will aim to overcome these limitations by exploring multi-bit metasurface architectures and incorporating time-modulation algorithms. Overall, the proposed wireless power transfer system demonstrates strong potential for further advancement and practical implementation in IoT applications.

Discussion

In summary, dynamically tuneable digital metasurfaces were integrated with LTCC micro-nano integration technology to construct a next-generation intelligent WPT system. A wideband integrated digital meta-atom was designed to surpass the bandwidth limitations of conventional resonant structures, achieving a relative bandwidth of 22% and a phase modulation accuracy of 180° ± 5° within the 5.0–6.25

GHz range. Combined with FPGA-controlled coding manipulation, the system enables millisecond-level multi-beam reconfiguration. This millisecond-level reconfiguration is primarily attributed to the low-speed level-shifting components in the FPGA-based controller rather than to the intrinsic switching speed of the PIN diodes or the FPGA clock rate. By leveraging a surface-plasmon-enhanced coupling mechanism and the synergistic optimisation of multilayer LTCC technology, we developed a compact 18 mm× 18 mm rectenna that can achieve an RF-to-DC conversion efficiency of 70.5% at 5.8 GHz, effectively addressing the efficiency degradation challenges in miniaturised receiving ends. Note that the term surface plasmon-enhanced coupling used in this study does not refer to true optical surface plasmon polaritons. Instead, it describes an equivalent surface-bound electromagnetic coupling mechanism arising from the strong confinement of surface currents and near-field energy at the metal–dielectric interfaces enabled by the multilayer metal–ceramic structure. This cross-scale synergistic design paradigm, which integrates electromagnetic manipulation with micro-nano manufacturing, provides a fabrication-compatible technological pathway for highly adaptable wireless power networks, advancing the practical deployment of self-powered IoT systems.

Materials and Methods

Experimental setup

The 64-element integrated digital metasurface was fabricated using conventional multilayer PCB technology. The radiation characteristics were evaluated in the far-field region within a microwave-anechoic environment. The experimental setup and test environment are illustrated in **Fig. S3**, where the metasurface prototype and its supporting metal frame were mounted on a computer-controlled rotation platform. The FPGA controller was fixed to the metallic frame of the metasurface and connected to the metasurface array using flexible flat cables. The rotation speed was synchronised with the spectrum analyser to enable accurate acquisition of the

harmonic radiation patterns. A standard horn antenna connected to an SG was used as the transmitting antenna, and the metasurface under test was connected to a spectrum analyser and acted as the receiving antenna. The radiation power pattern of the metasurface was obtained by comparing the received signal strength with that of a reference horn antenna. The measured performance results of the metasurface array are shown in **Fig. S4**.

The experimental environment and setup of the WPT system are shown in Fig. 4a a. An SG (Ceyear 1435F) and PA were used as the feed to generate a 5.8 GHz 36 dBm power signal. The receivers were placed 40 cm from the geometric centre of the metasurface to receive the beam power, and the receiving RF power level was calculated using the DC output voltage of the rectenna.

Numerical simulation

Performance simulations of the proposed meta-atom and metasurface array were performed using the full-wave electromagnetic field time-domain simulation algorithm—finite integration technique based on CST Microwave Studio. The meta-atom was simulated using a time-domain solver with a period of 25 mm× 25 mm and periodic boundary conditions. A 50-Ω discrete port was placed at the feed of the meta-atom to stimulate and obtain the performance characteristics. Furthermore, based on the designed meta-atom, an 8×8 metasurface array was constructed along with a uniform-phase feeding network at the bottom. Each PIN diode on the metasurface is encoded, with the conductive state represented as resistive (R = 5.2 Ω) and the off state as capacitive (C_{on} = 0.025 pF). Single-, dual-, or quad-beam radiation can be successfully achieved by applying different quantised phase coding distributions.

Sample fabrication based on LTCC

The rectenna was fabricated using the LTCC process with Ferro-A6M green tape as the dielectric substrate. The Ferro-A6M exhibits superior high-frequency

characteristics, featuring an exceptionally low dielectric loss ($\tan\delta$ = 0.002) and stable permittivity (ε_r = 5.9 ± 0.1) across frequency range from 1 to 100 GHz, thereby effectively minimising signal transmission loss while enhancing both antenna radiation efficiency and power conversion efficiency of the rectification. A 32-layer green tape stacking configuration was implemented, with each layer maintaining a precise thickness of 96 μm. Furthermore, the LTCC substrate demonstrates enhanced thermal management capabilities, possessing a thermal conductivity of approximately 2 $W \cdot m^{-1} \cdot K^{-1}$, which is significantly higher than organic substrates such as FR4 (0.3 $W \cdot m^{-1} \cdot K^{-1}$) or Rogers 4350B (0.69 $W \cdot m^{-1} \cdot K^{-1}$).

Acknowledgements

This research was supported by the National Natural Science Foundation of China under Grants 62471399 and 62401474, Gusu Leading Talents of Innovation and Entrepreneurship under Grant ZXL2024332, and Key Research and Development Program of Shaanxi under Grant 2024GX-YBXM-020.

Author Contributions

X. B. and X. G. supervised the study. H. Z. and Z. L. conceived the experiments. Y. D. and Y. C. designed the experimental setup. Z.L. performed the experiments. Y. Y. and L. S. developed the numerical methods for the simulation. All authors participated in the data analysis and contributed to the writing of the manuscript.

Conflict of interest

The authors declare no competing interests.

Supplementary information

Supplementary materials are available at the online version.

Data Availability Statement

Data supporting the findings of this study are available from the corresponding author upon request.

References

1. Tao, X. et al. Q. An active multi-beam antenna design method and its application for the future 6G satellite network. *Space: Science & Technology* **4**, 0149 (2024).

2. Liu, H. S. et al. Near-space communications: The last piece of 6G Space–Air–Ground–Sea integrated network puzzle. *Space: Science & Technology* **4**, 0176 (2024).

3. Lu, W. D. et al. Collaborative energy and information transfer in green wireless sensor networks for smart cities. *IEEE Transactions on Industrial Informatics* **14**, 1585-1593 (2018).

4. Trevisan, R. & Costanzo, A. A UHF near-field link for passive sensing in industrial wireless power transfer systems. *IEEE Transactions on Microwave Theory and Techniques* **64**, 1634-1643 (2016).

5. Liao, Y. H. et al. Integration of communication and navigation technologies toward LEO-enabled 6G networks: a survey. *Space: Science & Technology.* **3**, 0092 (2023).

6. Wei, Z. D. et al. A hybrid RF and solar integrated energy harvesting system using optically transparent metasurface. *IEEE Transactions on Antennas and Propagation* **73**, 920-927 (2025).

7. Li, X. F. et al. A robust wireless power transfer system with self-alignment capability and controllable output current for automatic-guided vehicles. *IEEE Transactions on Power Electronics* **38**, 11898-11906 (2023).

8. Huang, J. et al. Wireless power transfer and energy harvesting: current status and future prospects. *IEEE Wireless Communications* **26**, 163-169 (2019).

9. Zhang, Y. M. et al. Integration of onboard charger and wireless charging system for electric vehicles with shared coupler, compensation, and rectifier. *IEEE Transactions on Industrial Electronics* **70**, 7511-7514 (2023).

10. Patil, D. et al. Wireless power transfer for vehicular applications: overview and challenges. *IEEE Transactions on Transportation Electrification* **4**, 3-37 (2018).

11. Chen, X. M., Ng, D. W. K. & Chen, H. H. Secrecy wireless information and power transfer: challenges and opportunities. *IEEE Wireless Communications* **23**, 54-61 (2016).

12. Cui, T. J. et al. Coding metamaterials, digital metamaterials and programmable metamaterials. *Light*: *Science & Applications* **3**, e218 (2014).

13. Bai, X. D. et al. High-efficiency transmissive programmable metasurface for multimode OAM generation. *Advanced Optical Materials* **8**, 2000570 (2020).

14. Zhang, J. R. et al. Multidimensional multiplexing geometric phase metaholography. *Light*: *Advanced Manufacturing* **6**, 474-485 (2025).

15. Bai, X. D. et al. Radiation-type programmable metasurface for direct manipulation of electromagnetic emission. *Laser & Photonics Reviews* **16**, 2200140 (2022).

16. Wang, L. P. et al. Ultra-wideband transmissive programmable metasurface enabled near-field holography and far-field OAM generation. *Laser & Photonics Reviews* **20**, e01020 (2026).

17. Gao, T. S. et al. Space-time-modulated radiation-type digital metasurface enabled smart jamming. *Laser & Photonics Reviews* **20**, e01421(2026).

18. Zhang, L. & Cui, T. J. Space-time-coding digital metasurfaces: principles and applications. *Research* **2021**, 9802673 (2021).

19. Bai, X. D. et al. Wideband radiation-type programmable metasurface-enabled high-precision beam modulating for IoT applications. *IEEE Internet of Things Journal* **12**, 28823-28834 (2025).

20. Zhou, J. F. et al. Metamaterials and metasurfaces for wireless power transfer and energy harvesting. *Proceedings of the IEEE* **110**, 31-55 (2022).

21. Bai, X. D. et al. Dynamic millimeter-wave OAM beam generation through programmable metasurface. *Nanophotonics* **11**, 1389-1399 (2022).

22. Li, Y. X. et al. Achiral light-controlled coding metasurfaces with multi-channel electromagnetic control. *Light*: *Advanced Manufacturing* **6**, 120-129 (2025).

23. Cao, A. J. et al. Conformal radiation-type programmable metasurface for agile millimeter-wave orbital angular momentum generation. *Research* **8**, 0631 (2025).

24. Chen, Y. H. et al. Ka-Band cross-shaped reconfigurable metasurface antenna for agile beam modulation. *IEEE Transactions on Antennas and Propagation* **73**, 6127-6132 (2025).

25. Jo, S., Lee, W. & Lee, H. Metasurface patch for wireless power transfer in implantable devices. *Advanced Functional Materials* **33**, 2300027 (2023).

26. Meng, Z. K. et al. Voice interactive information metasurface system for simultaneous wireless information transmission and power transfer. *npj Nanophotonics* **1**, 12 (2024).

27. Liu, H. X. et al. Multitarget simultaneous wireless information and power transfer (SWIPT) scheme based on anisotropy-metasurface field synthesis. *IEEE Transactions on Antennas and Propagation* **72**, 8466-8475 (2024).

28. de Almeida, J. V. et al. Nonlinear metasurfaces for health-monitoring magnetic induction-based SWIPT base stations. *IEEE Transactions on Microwave Theory and Techniques* **71**, 309-319 (2023).

29. Li, L. et al. Efficient wireless power transfer system integrating with metasurface for biological applications. *IEEE Transactions on Industrial Electronics* **65**, 3230-3239 (2018).

30. Gong, S. Q. et al. Beamforming optimization for intelligent reflecting surface-aided SWIPT IoT networks relying on discrete phase shifts. *IEEE Internet of Things Journal* **8**, 8585-8602 (2021).

31. Yu, F. et al. Compact shared aperture metasurface with power splitting for simultaneous wireless information and power transfer. *IEEE Internet of Things Journal* **12**, 14386-14397 (2025).

32. Xia, D. X. et al. Adaptive wireless-powered network based on CNN near-field positioning by a dual-band metasurface. *Nature Communications* **15**, 10358 (2024).

33. Chang, M. Y. et al. Tailless information–energy metasurface. *Advanced Materials* **36**, 2313697 (2024).

34. Wang, X. et al. High-performance cost efficient simultaneous wireless information and power transfers deploying jointly modulated amplifying

programmable metasurface. *Nature Communications* **14**, 6002 (2023).

35. Tian, S. C. et al. Recent advances in metamaterials for simultaneous wireless information and power transmission. *Nanophotonics* **11**, 1697-1723 (2022).

36. Chu, Z. Y. et al. On propagation loss for reconfigurable surface wave communications. *IEEE Transactions on Communications* **73**, 1547-1559 (2025).

37. Zhang, P., Zhang, X. M. & Li, L. An optically transparent metantenna for RF wireless energy harvesting. *IEEE Transactions on Antennas and Propagation* **70**, 2550-2560 (2022).

38. Bai, X. D. et al. Time-modulated transmissive programmable metasurface for low sidelobe beam scanning. *Research* **2022**, 9825903 (2022).

39. Wang, L. P. et al. Reconfigurable metasurface-driven pixel-wise visual cryptography for high-security dynamic encryption. *Laser & Photonics Reviews* **n/a**, e02960 (2026).

40. Wang, L. P. et al. Temporal integral holography with intelligent metasurface. *Photonics Research* **15**, 592257 (2026).

41. Rotenberg, S. A. et al. Efficient rectifier for wireless power transmission systems. *IEEE Transactions on Microwave Theory and Techniques* **68**, 1921-1932 (2020).

42. Kim, J. & Clerckx, B. Wireless information and power transfer for IoT: pulse position modulation, integrated receiver, and experimental validation. *IEEE Internet of Things Journal* **9**, 12378-12394 (2022).

43. Halimi, M. A. et al. Rectifier circuits for RF energy harvesting and wireless power transfer applications: a comprehensive review based on operating

conditions. *IEEE Microwave Magazine* **24**, 46-61 (2023).

44. Aboualalaa, M., Mansour, I. & Pokharel, R. K. Energy harvesting rectenna using high-gain triple-band antenna for powering internet-of-things (IoT) devices in a smart office. *IEEE Transactions on Instrumentation and Measurement* **72**, 2001312 (2023).

45. Zada, M. et al. Empowering remote patient monitoring with a dual-band implantable rectenna system for wireless power and data transfer. *IEEE Transactions on Antennas and Propagation* **71**, 9509-9522 (2023).

46. Kumar, M. et al. A planar integrated rectenna array with 3-D-spherical DC coverage for orientation-tolerant wireless-power-transfer-enabled IoT sensor nodes. *IEEE Transactions on Antennas and Propagation* **71**, 1285-1294 (2023).

47. Battistini, G. et al. A novel 3-D printed dual-port rectenna for simultaneous energy harvesting and backscattering of a passively generated UWB pulse. *IEEE Transactions on Microwave Theory and Techniques* **72**, 812-821 (2024).

48. Chou, H. T. et al. LTCC-based dual-polarized AiP module by multilayered cross-dipole antennas for 5G mobile terminal applications at 28 GHz Band. *IEEE Transactions on Components*, *Packaging and Manufacturing Technology* **13**, 1663-1672 (2023).

49. Zhou, C. Y. et al. Millimeter-wave wideband dual-polarized LTCC antenna array based on metasurfaces for beam-scanning applications. *IEEE Transactions on Antennas and Propagation* **70**, 9912-9917 (2022).

50. Chen, Z. N. et al. Microwave metalens antennas. *Proceedings of the IEEE* **111**, 978-1010 (2023).

51. CST Microwave Studio. Workflow & Solver Overview. (CST Microwave

Studio, 2008).

52. Yu, H. et al. Quad-polarization reconfigurable reflectarray with independent beam-scanning and polarization switching capabilities. *IEEE Transactions on Antennas and Propagation* **71**, 7285-7298 (2023).

53. Tian, J. et al. Wideband transmissive programmable metasurface for adaptive millimeter-wave beamforming. *Laser & Photonics Reviews* **19**, 2401333 (2025).

54. Pozar, D. M. Microwave Engineering. *Wiley* (2011).